J. Fluid Mech. (1990), *vol.* 218, *pp.* 463–482
Printed in Great Britain

Structure of large-scale vorticity in a turbulent far wake

By D. K. BISSET, R. A. ANTONIA AND D. BRITZ†
Department of Mechanical Engineering, University of Newcastle, NSW, 2308, Australia

(Received 20 September 1989 and in revised form 15 February 1990)

Simultaneous measurements have been made of large-scale approximations of the three components of the vorticity vector in the far wake of a slightly heated cylinder. Analysis of the results is directed towards the properties of large-scale spanwise vortices and shear-aligned double-roller vortices and the relationship between them. The relationship between vorticity and temperature is also studied. The probability density function of the inclination of the vorticity vector in the (x, y)-plane exhibits a maximum at about 45° in the central part of the wake. The p.d.f. of the inclination of the vorticity vector in the (x, z)-plane supports the existence of a concentration of spanwise vorticity near the outer part of the wake. In this region, there is significant correlation between vorticity and temperature. Conditional averages of velocity and temperature fluctuations and vorticity components are presented with respect to two types of detection, the first focusing on peaks in the ω_x and ω_y signals, and the second focusing on aspects of the large spanwise structures. Results from the two procedures are consistent, although different in emphasis, and are interpreted in terms of the downstream development of the wake. The upstream ends of large structures stretch and shear-align smaller, probably older, vortices while transporting heat and momentum defect outwards. Near the centreplane, the downstream ends of large structures transport colder, high-speed, spanwise-vortical fluid towards the centreplane, but ω_x and ω_y are not correlated with either temperature or the large structure. In (x, z)-planes, cuts through the shear-aligned vortices would appear to show double rollers.

1. Introduction

The description of the organized motion in the fully developed far wake has generally been in terms of two types of structures. The first type consists of contrarotating double-roller vortices with circulation mainly in the (x, z)-plane (coordinate axes are shown in figure 1). These vortices have parallel axes which are displaced in the z- or spanwise direction and are approximately aligned in the principal direction of mean strain (Grant 1958; Payne & Lumley 1967; Mumford 1983; Ferre & Giralt 1989*a*, *b*). The second type refers to spanwise vortices (Keffer 1965; Townsend 1979; Mumford 1983) sometimes described as mixing jets or entraining eddies with circulation mainly in the (x, y)-plane.

Useful information has been gleaned about various properties of each type of structure. For example, Mumford (1983) found that the double-roller vortices are often confined to one side of the centreline and tend to occur in pairs or longer groups with their centres separated in the x-direction. Ferré & Giralt (1989*a*) concluded that

† Permanent address: Kemisk Institut, Aarhus Universitet, DK-8000, Aarhus, Denmark.

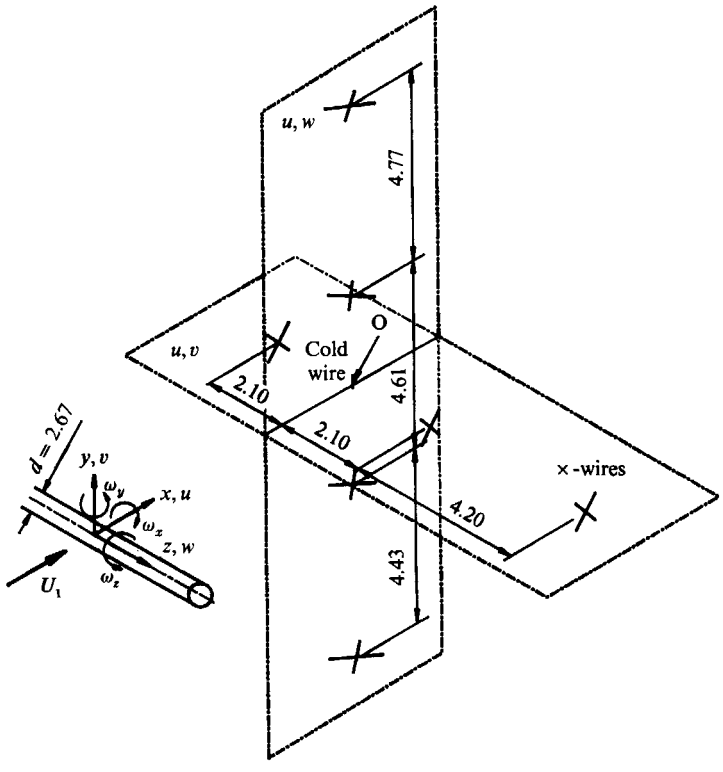

FIGURE 1. Definition diagram and sketch of vorticity/temperature probe. Dimensions are in mm.

double-roller eddies occupy 50% of the flow and contain approximately the same fraction of the u-component energy, irrespective of initial conditions. Townsend (1979) showed that the spanwise vortices tend to occur in groups of between three and five individual structures, with a reasonably uniform streamwise spacing within any particular group. The most common arrangement of spanwise vortices is one that is alternating with respect to the centreline, although other arrangements also occur (Bisset, Antonia & Browne 1990).

The possibility that the two types of vortices are interconnected has been raised by several authors (Grant 1958; Roshko 1976; Savill 1979; Mumford 1983). Savill (1979) suggested that double rollers and spanwise structures may form different parts of a horseshoe-type vortex. Mumford noted that only indirect evidence existed for the outer ends of the double-roller structures being joined by the spanwise rollers. He suggested that the similarity between the streamwise groupings of the double-roller and spanwise structures could be taken as stronger evidence for the connection between the two types of structures. He also suggested that the straining in the (x, y)-plane that is induced by consecutive spanwise structures could result in the formation of double-roller structures. Recently, Hayakawa & Hussain (1989) have suggested that horseshoe-like structures and/or a braid of longitudinal vortices are responsible for strong three-dimensionality in the wake much nearer to the cylinder.

Some information about the large-scale spanwise vorticity field of the far wake was obtained in our laboratory using an array of ×-probes aligned in the (x, y)-plane (Bisset *et al.* 1990). Data from the same array rotated through 90° so that the probes were in the (x, z)-plane provided good support for the double-roller structures (Ferré,

Giralt & Antonia 1989). However, a direct connection between the two types of structure has not been found although it is not ruled out by these data or by the flow visualizations presented in Antonia *et al.* (1987*a*). The present investigation was aimed at providing information on the three-dimensional large-scale vortical field in the far wake, primarily to shed some light on the possible connection between the double roller and spanwise vortical structures. A second aim is to explore the connection between the three-dimensional vortical field and the temperature fluctuations in the far wake of a slightly heated cylinder.

The experimental methodology is described in §2, details of how the large-scale vorticity components are calculated are given in §3, while detection and conditional averaging procedures are outlined in §4. Results for statistics of vorticity and temperature fluctuations are given in §5, and §6 contains statistics of the angles between components of the vorticity vector. Results based on two kinds of detection and conditional averaging are given in §7, one focusing on longitudinal and transverse vorticity components and the other focusing on relatively large-scale spanwise structures. The interrelationships between these results, and a possible physical explanation in terms of downstream development of the wake, are discussed in §8.

2. Experimental details

Measurements were made in an open-return low-turbulence wind tunnel with a working section of 350 mm × 350 mm, 2.4 m long. The wake was generated by a cylinder of diameter $d = 2.67$ mm spanning the width of the working section. The bottom wall of the working section was slightly tilted to maintain a zero pressure gradient. The cylinder was heated electrically, the heat input being sufficiently small for temperature to be treated as a passive marker of the far-wake flow, as discussed in Antonia *et al.* (1987*a*). The present experimental conditions are identical to those used in previous work (Browne, Antonia & Bisset 1986; Antonia *et al.* 1987*a*).

The free-stream velocity U_1 was 6.7 m/s and the Reynolds number, based on U_1 and d, was 1170. The free-stream turbulence was estimated to be about 0.05%. All measurements were made at $x/d = 420$, where x is the streamwise distance measured from the cylinder. At this location, the mean velocity half-width L is 12.3 mm, the centreline mean velocity defect U_0 is 0.36 m/s, while the mean temperature excess T_0 at the centreline is 0.8 K. An asterisk denotes normalization by L, U_0 and T_0.

The arrangement used for the simultaneous determination of three (large-scale) components of vorticity is sketched in figure 1. It comprises four ×-wires parallel to the (x, z)-plane and aligned in the y-direction as well as three ×-wires which are parallel to the (x, y)-plane and aligned in the z-direction. A cold wire is located at point O, the nominal intersection of the two lines of ×-wires. All the wires in the arrangement sketched in figure 1 form an integral part of the same probe which was traversed in the y-direction† at $x/d = 420$.

The hot wires (5 μm diameter, Pt–10% Rh) were operated at an overheat of 0.6 with constant-temperature circuits built in-house. The cold wire (0.63 μm diameter) was operated in a constant-current circuit, with the current set at 0.1 mA. The signals from all circuits were offset, amplified and then digitized using a 16 channel, 12 bit data acquisition system, at a sampling frequency F_s of 2564 Hz per channel (filter cutoff frequency = 1250 Hz) into a PDP 11/34 computer. Using velocity/yaw

† Unfortunately a computer malfunction caused the loss of the data file at $y^* = 0.98$ after some of the experimental equipment had been removed for use elsewhere.

calibrations and the measured temperature coefficient of the cold wire (1.69×10^{-3} K^{-1}), signals proportional to the velocity fluctuations u, v and w and to the temperature fluctuation θ were formed and stored on digital tape. The mean velocity $\bar{U}$ corresponding to the voltage from each hot wire was obtained using a microcomputer with data-logging system connected directly to the output of each anemometer. Subsequent processing of the data was carried out on a VAX 8650 computer.

3. Formation of vorticity components

The vorticity components are defined in terms of derivatives of the instantaneous velocities U, V and W. Since $\bar{V}$ and $\bar{W}$ are negligible and $\partial(\bar{U})/\partial z$ is zero, the components can be redefined in terms of velocity fluctuations as follows:

$$\omega_x = \frac{\partial w}{\partial y} - \frac{\partial v}{\partial z}, \tag{1a}$$

$$\omega_y = \frac{\partial u}{\partial z} - \frac{\partial w}{\partial x}, \tag{1b}$$

$$\omega_z = \frac{\partial v}{\partial x} - \frac{\partial u}{\partial y} - \frac{\partial \bar{U}}{\partial y}. \tag{1c}$$

The velocity fluctuations were digitally filtered using a moving least-squares parabolic fit, with a cutoff frequency of $0.15F_s$. This was necessary to eliminate contamination of the derivatives with noise, i.e. fluctuations resulting from small-scale turbulence that cannot be resolved with the present spacing between $\times$-wires. For consistency in subsequent data processing, θ was similarly filtered, which reduced the variance of θ by about 2%.

Again owing to the coarse spacing, higher-order derivative approximations such as least-squares or spline fitting to all three or four available $\times$-wire points along z or y, respectively, did not improve the results, and simple central finite differences between the respective two points on either side of the probe centre in z and y were employed. For the two derivatives in x, Taylor's hypothesis was invoked: for example, for v,

$$\frac{\partial v}{\partial x} \approx -\frac{1}{\bar{U}} \frac{\partial v_0}{\partial t}, \tag{2}$$

where v_0 is the interpolated value of v at the effective probe centre, formed as the mean of the two v-values on either side of the centre in the z-direction. The derivative $\partial v_0/\partial t$ at time $k\Delta t$ was computed as $[v_0(k+1) - v_0(k-1)]/2\Delta t$, k here being the index to sampling time intervals. Since the local turbulence intensity is quite small at the measurement station, it is expected that Taylor's hypothesis is reasonable. The value of $2\bar{U}\Delta t$ is very similar to the spacing between adjacent probes, i.e. $\Delta x \approx \Delta y \approx \Delta z$. The values of $\partial \bar{U}/\partial y$ used for ω_z were computed from a least-squares cubic spline fit to a set of calibration points $\bar{U}(y)$.

When velocities at the probe centre were required they were obtained, as mentioned above for v_0, as the mean of the measured velocities on either side of the centre. Several tests were done to ensure that these interpolated signals were reasonable. For a given probe location, all v-signals and some of the u-signals are at the same value of y, allowing direct comparison. It was also possible to find a few probe locations where a given $\times$-wire position (in y) closely matched that of the

effective probe centre at another probe location, thus allowing comparison of w_0-with w-signals. Normalized spectra of these matched signals showed close agreement. Spectra of u_0 computed by interpolation along either the y-axis or the z-axis agreed well with the equivalent spectrum of u. In this sense, then, the probe-centre interpolated signals could be regarded as satisfactory. Their root-mean-square values, however, were generally smaller than those of the surrounding velocities by a factor of around 0.7. This is again a consequence of the coarse spacing and the fairly low correlations between adjacent probe points: for example, the two $u(y)$-signals on either side of the probe centre at $y^* = 0.65$ gave a correlation coefficient of 0.27, while the $u(z)$-signals yielded 0.57. But the two u_0 signals formed from these different pairs had a strong correlation of 0.8 with each other. The $v(z)$-signals were always well correlated (correlation coefficient 0.5 to 0.7). The coefficients for $w(y)$ were much lower (≈ 0.1), but the r.m.s. values of w_0 were only slightly lower than expected relative to v_0 at the same y. The overall conclusion from normalized spectra, correlation coefficients and r.m.s. values is that interpolation is adequate in the context of the present study.

4. Detections and conditional averages

Two kinds of detections were made, namely positive or negative peaks in vorticity components, and large-scale changes in the value of the v_0 signal. The former are important because it is very rare to have all three components of vorticity available for detection purposes, but the latter are also important because they allow the present data to be related to previous results using similar methods.

A detection of a positive vorticity peak is the point of maximum vorticity in between upward and downward crossings of a threshold level, and a detection of a negative vorticity peak is the analogous minimum. Detections in the v_0 signal were made using the WAG method described in Antonia & Fulachier (1989) and Bisset *et al.* (1990). Briefly, the WAG function is defined as the difference between the mean values of two successive short lengths of the signal, multiplied by either $+1$ or -1 depending on which direction of change in the signal is required. Detection regions are found, beginning when the WAG function exceeds a threshold and ending when it becomes negative. A detection is the point at which the WAG function is maximum in a detection region. For both detection methods the thresholds were adjusted so that there were approximately 3600 detections (fewer in the outer part of the wake), which, for the present record duration, corresponds to the frequency of the peak in the power spectrum of v at all y-values.

Conditional averages were formed in the usual way, i.e.

$$\langle \alpha \rangle_k = \frac{1}{n} \sum_{i=1}^{n} \alpha(j_i + k), \tag{3}$$

where the j_i are the n detection points. The subscript k is usually omitted. The conditional averages presented in this paper are all based on selected subsets of detections, but the selection criteria are described in §7.

5. Statistics of ω_x, ω_y, ω_z and θ

Distributions of ω_x', ω_y', ω_z' and θ' are shown in figure 2, where a prime denotes an r.m.s. quantity. Also shown in the figure is the distribution of the r.m.s. value of ω,

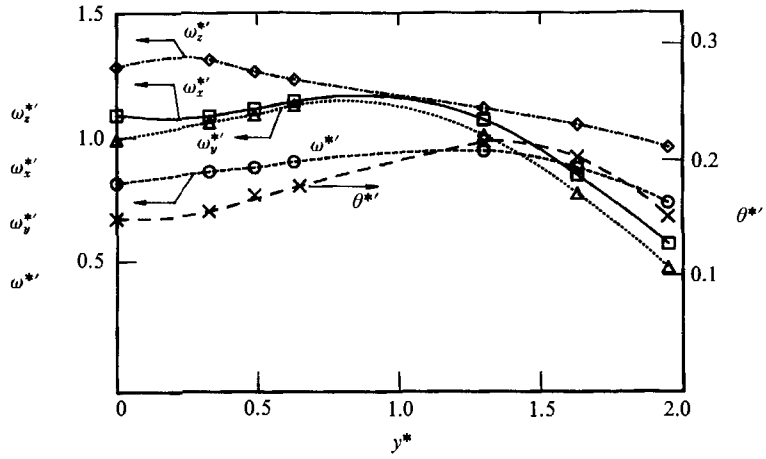

FIGURE 2. Distribution of r.m.s. values: □, $\omega_x^{*\prime}$; △, $\omega_y^{*\prime}$; ◇, $\omega_z^{*\prime}$; ○, $\omega^{*\prime}$; ×, $\theta^{*\prime}$.

the magnitude of the vorticity vector, viz. $\omega = (\omega_x^2+\omega_y^2+\omega_z^2)^{\frac{1}{2}}$. The distributions of ω_x' and ω_y' follow each other sufficiently closely to suggest that ω_x' and ω_y' are approximately equal. Both ω_x' and ω_y' first increase away from the centreline up to a maximum near $y^* \approx 1$ before decreasing towards the edge of the wake. By contrast, ω_z' has its peak near or at the centreline and decreases relatively slowly towards the edge of the wake; its magnitude remains everywhere larger than ω_y' (or ω_x'). Note that the relative behaviour of ω_z' and ω_y' shown in figure 2 is qualitatively similar to that reported in Antonia, Browne & Shah (1988). In that paper however, ω_x' was greater than ω_y', possibly due to the method used in approximating its value ($\omega_x \approx [\overline{\{\partial w/\partial y\}^2}+\overline{\{\partial v/\partial z\}^2}]^{\frac{1}{2}}$).

Qualitatively, the variation of ω' follows that of ω_y' (or ω_x') near the centreline of the flow and that of ω_z' towards the outer wake region. The peak value of ω' occurs at approximately the location at which θ', the r.m.s. temperature, is highest. The y^* location of this peak is significantly higher than 0.9, the value at which the mean vorticity $(\partial\bar{U}/\partial y)$ is maximum.

Correlation coefficients have been estimated for various combinations of vorticity and temperature fluctuations. The standard definition of the correlation coefficient is used, viz.

$$\rho_{\alpha\beta} = \frac{\overline{(\alpha-\bar{\alpha})(\beta-\bar{\beta})}}{\overline{(\alpha-\bar{\alpha})^2}^{\frac{1}{2}}\overline{(\beta-\bar{\beta})^2}^{\frac{1}{2}}} \tag{4}$$

where $\alpha, \beta \equiv \omega_x, \omega_y, \omega_z, \omega$ or θ. Figure 3 shows that there is a significant correlation between ω_x and ω_y throughout much of the wake. Symmetry considerations require that correlation coefficients between ω_z and either ω_x or ω_y should be zero. The measured values (not shown) are small although, in a few cases, they approach ± 0.1.

Correlation coefficients between vorticity and temperature were also measured. Symmetry with respect to the z-direction requires that correlations between ω_x or ω_y and the scalar fluctuation θ should be zero. This is generally confirmed by the measured values of $\rho_{\omega_x\theta}$ and $\rho_{\omega_y\theta}$ (not shown). The correlation coefficient $\rho_{\omega_z\theta}$ (figure 3) has a positive peak near $y^* \approx 0.5$ and changes sign at $y^* \approx 1.2$. The largest negative values occur near the edge of the wake; in this region, $\rho_{\omega\theta}$ is slightly larger than the magnitude of $\rho_{\omega_z\theta}$.

The negative values of $\rho_{\omega_z\theta}$ in the outer part of the wake indicate that spanwise

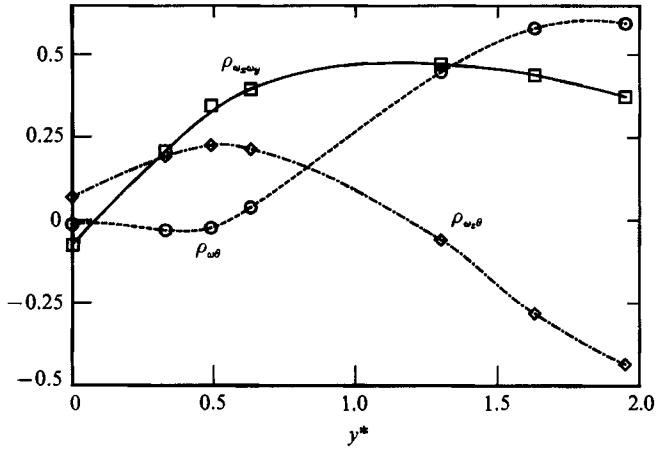

FIGURE 3. Correlation coefficients between ω_x and ω_y, ω_z and θ, ω and θ for the upper half of the wake: □, $\rho_{\omega_x\omega_y}$; ◇, $\rho_{\omega_z\theta}$; ○, $\rho_{\omega\theta}$.

vorticity mainly resides in relatively warm fluid moving towards the wake edge. Observations of dye in the far wake of a cylinder (Antonia *et al.* 1987*a*) suggested a reasonably high correlation between dye concentrations in the outer wake and spanwise vorticity, as inferred from the paths of dye streaklines introduced just outside the edge of the wake. The positive values of $\rho_{\omega_z\theta}$ in the region $0 < y^* \lesssim 1.2$ indicate that, in fully turbulent zones, spanwise vorticity resides in relatively cold, high-momentum fluid, probably entrained by the organized motion. In this region, the temperature is negatively skewed, while it is positively skewed in the outer region of the wake. Near the centreline, the correlation coefficient $\rho_{\omega\theta}$ is small compared with $\rho_{\omega_z\theta}$, although both coefficients tend towards zero at $y^* = 0$. In the outer region $\rho_{\omega\theta}$ is large, i.e. vorticity is associated strongly with warm fluid.

6. Inclination of the vorticity vector

The instantaneous projection angles of the vorticity vector onto the (x, y)-, (x, z)- and (y, z)-planes were calculated at several positions across the wake. These angles are defined as follows:

$$\alpha = \tan^{-1}\left[\frac{\omega_y}{\omega_x}\right], \tag{5a}$$

$$\beta = \tan^{-1}\left[\frac{\omega_z}{\omega_x}\right], \tag{5b}$$

$$\gamma = \tan^{-1}\left[\frac{\omega_y}{\omega_z}\right]. \tag{5c}$$

The sign convention for these angles is shown in figure 4 while distributions of the probability density function p of these angles are given in figures 5, 6 and 7 for several values of y^*.

On the centreline, $p(\alpha)$ has slight peaks at $\alpha = 0$ and $\alpha = \pm 180°$ (figure 5). At a short distance away from the centreline $p(\alpha)$ exhibits significant peaks at $\alpha \approx 45°$ and $\alpha = -135°$. In the outer edge of the wake these peaks shift towards $\alpha = 20°$ and $\alpha = -160°$. Except for regions near the centreline and at the edge of the wake, the

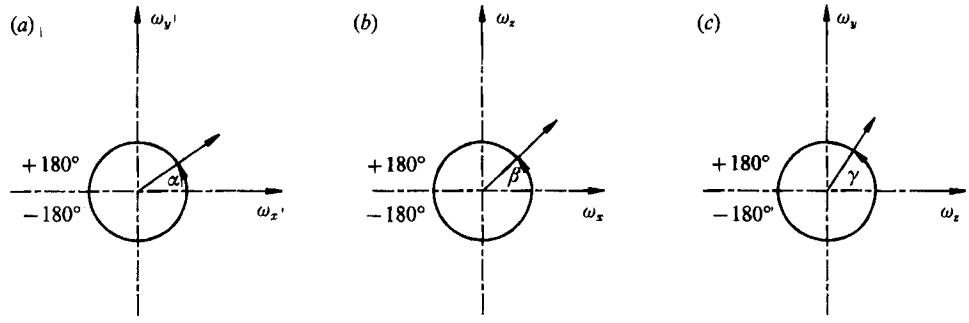

FIGURE 4. Convention used for angles α, β and γ; (a) α; (b) β; (c) γ.

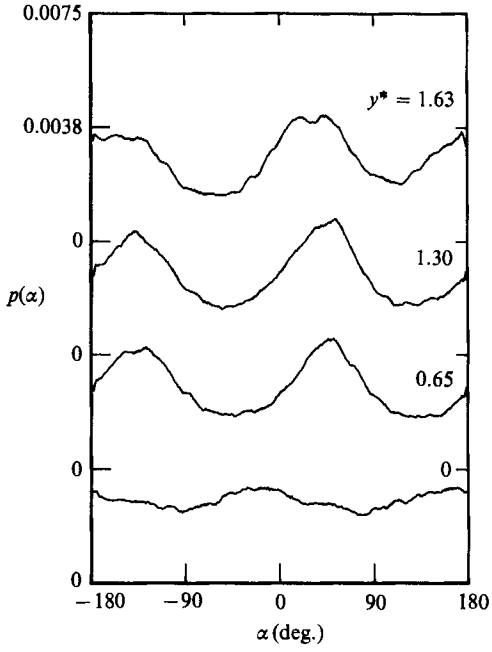

FIGURE 5. Probability density function of α, where $\tan\alpha = \omega_y/\omega_x$.

behaviour of $p(\alpha)$ supports the notion of vortices that are stretched mainly at an angle of 45° in the (x, y)-plane. This angle corresponds approximately to the direction of the principal rate of strain. Deissler (1969) showed that the angle at which $\overline{\omega_x^2}$ is maximum is 45°, but this maximum is achieved only when $\overline{\omega_x^2} = \overline{\omega_y^2}$ (i.e. for isotropic turbulence). He also found that, in a weak homogeneous flow with a uniform transverse velocity gradient, this angle is close to the direction of maximum mean strain rate for a range of velocity gradients. The condition $\overline{\omega_x^2} = \overline{\omega_y^2}$ is approximately satisfied by the present results (figure 2) although the turbulence is not isotropic. The peak of $p(\alpha)$ at $\alpha = 45°$ is not sharp but rather broadly distributed. The distribution is quite similar to that calculated by Moin & Kim (1985) from a database generated by applying the large-eddy simulation technique to a turbulent channel flow. With the exclusion of regions near the wall and near the centre of the duct, the inclination angle of the vorticity vector was found to be about 45° to the wall. Direct evidence was provided for the existence of vortical structures at the same inclination. These authors noted that the 180° period of their histograms is simply a consequence of

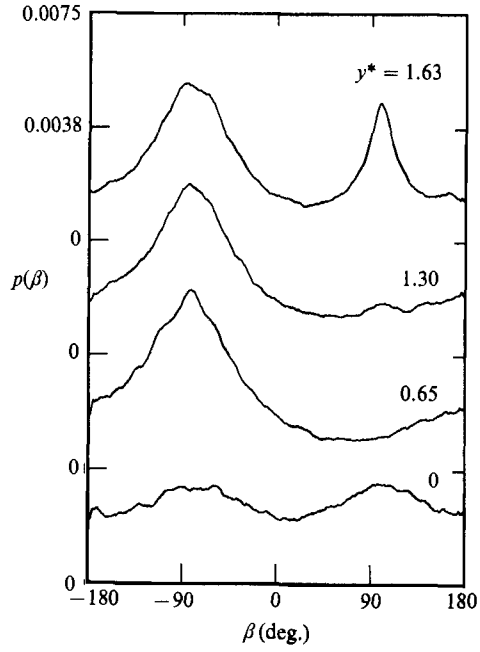

FIGURE 6. Probability density function of β, where $\tan\beta = \omega_z/\omega_x$.

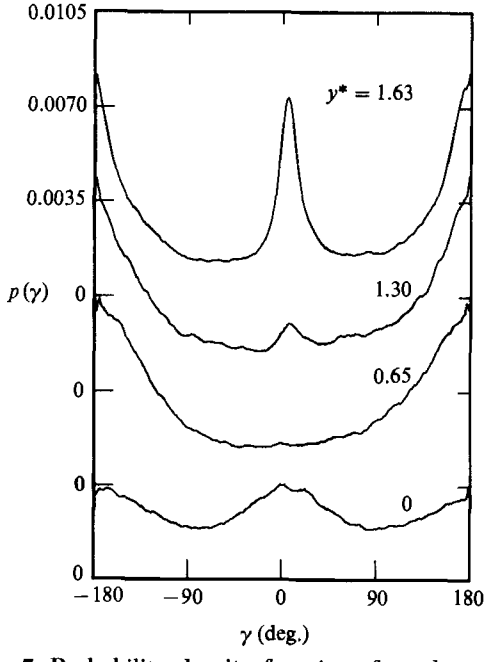

FIGURE 7. Probability density function of γ, where $\tan\gamma = \omega_y/\omega_x$.

invariance with respect to reflection of the z-axis (both ω_x and ω_y change sign after reflection). This observation also applies to the present data: in particular, it precludes the argument that the peak at $\alpha = -135°$ necessarily reflects the presence of the second leg of a hairpin-like vortex structure.

The distribution of $p(\beta)$ differs from that of $p(\alpha)$ in that the 180° period of figure

5 is absent in figure 6 for intermediate values of y^*; only ω_x (and not ω_z) changes sign following reflection of the z-axis. On the centreline, $p(\beta)$ appears to be symmetrical about $\beta = 0$ and shows slight peaks at $\beta = \pm 90°$. In this region, the mean of ω_z is nearly zero because of structures that originate both above and below the centreline, and ω_z' is larger than ω_x' (figure 2). As y^* increases, there is a broad peak at $\beta = -90°$, corresponding to predominantly negative spanwise vorticity from structures above the centreline. In the outer part of the wake, $\bar{\omega}_z$ is again nearly zero so that ω_z can assume either sign, explaining perhaps the emergence of a second, rather narrow, peak near $\beta = +90°$.

The distribution of $p(\gamma)$ is, as required, symmetrical about $\gamma = 0$ (figure 7). As y^* increases and ω_z is nearly always negative, the peak at $\gamma = 0$ declines by comparison to the peaks at $\pm 180°$. At larger y^* a narrow peak at $\gamma = 0$ appears. This peak corresponds to positive values of ω_z that mainly occur when ω_y is approximately zero.

7. Conditional velocity, temperature and vorticity distributions

Conventional statistics, such as those presented in §§5 and 6, describe certain aspects of the flow, but do not provide a clear physical picture of the underlying turbulent motion, especially the organized motion. Detection and conditional averaging methods constitute a more direct approach to the study of recurring physical features.

Conditional averages of vorticity components, temperature, velocities, etc. based on single-point detections (described in §4) in several different signals were calculated but are not presented here. They generally suffer from the problems that the conditional average of the quantity used for detection is exaggerated relative to the other conditional averages, and conditional averages rapidly become degraded at times other than the detection point (i.e. $k \neq 0$ in (3)). Also, symmetry about the (x, y)-plane means that conditional averages of certain quantities not used for detection will be necessarily zero.

Three methods of reducing the impact of these problems were used, sometimes in combination, all of which involve selecting subsets of detections that satisfy certain additional criteria, as follows.

(i) Independent detections in a second quantity were selected only when they occurred at the most probable times relative to detections in the first quantity.

(ii) Detections in a given quantity were selected when they were separated from other detections in the same quantity by the most probable time interval.

(iii) The sign of a quantity that exhibits symmetry about the (x, y)-plane, at a certain point in time relative to detections in another quantity, was used to split that set of detections into two 'symmetrical' subsets.

7.1. *Detections in ω_x and ω_y*

Above the centreline it was found that detections of positive peaks in ω_y most frequently occur about the same time as detections of positive peaks in ω_x. Therefore, sets of simultaneous detections of positive peaks in ω_x and ω_y were obtained (i.e. a detection in ω_x was accepted only if there was a detection in ω_y at the same time). Conditional averages of u_0, v_0, w_0, θ and ω_z for five y^* locations are shown in figure 8, and distributions of $\langle \omega_x \rangle$ and $\langle \omega_y \rangle$ are shown in figure 8(f) for $y^* = 1.3$ ($\langle \omega_x \rangle$ and $\langle \omega_y \rangle$ are similar for all y^* values). The conditional vorticity vector at the detection instant is shown schematically in figure 9(a). Negative peaks in ω_x and ω_y also tend to occur simultaneously, and the corresponding vorticity vector is shown in figure

9(*b*). Conditional averages (not shown) for this case are essentially unchanged except for $\langle w_0 \rangle$ which is the mirror image of $\langle w_0 \rangle$ in figure 8(*c*). At the detection instant the angle ϕ between $\langle \omega \rangle$ and the (x, y)-plane is about 10° at small y^*, and increases to about 25° for large y^*. The number of pairs of simultaneous detections is much smaller at large y^* because of intermittency, the number at $y^* = 1.95$ being only 20% of that at $y^* = 0.65$ or 1.30. Kim & Moin (1986) examined concentrations of vortex lines in a numerically simulated channel flow, and found that the vorticity vector actually represents a vortex of rotating fluid and not just a localized shear layer. In the present work, conditional averages (not shown) from the individual ×-wires lead to the same conclusion.

The results in figure 8 show that $\langle \omega \rangle$, when detected in this manner, is associated with relatively warm, rising, low-momentum fluid at large y^*, and at small y^* it is associated with descending, relatively high-momentum fluid whose temperature is unchanged from the local average. At large y^*, and very close to the centreline, the fluid producing the ω_x and ω_y detections is also relatively strong in spanwise vorticity ω_z. At immediate y^* the level of ω_z is no different from that in the surrounding fluid. There is no evidence here about how the detections at different y^* are aligned with each other, but it would be reasonable to align the detections along the associated vorticity vectors indicated in figure 9. The resulting vortices are generally consistent with the single- and double-roller models of Grant (1958) and Mumford (1983), but they are also consistent with the presence of hairpin vortices with legs nearly parallel. Examination of the velocities $(\langle u_0 \rangle + \bar{U}, \langle v_0 \rangle)$ at various positions along the assumed vortex indicates that the vortex is being stretched considerably, which tends to intensify the vorticity. The mechanism causing the stretching cannot be determined from these results. The fact that the angle of the vorticity vector with the (x, y)-plane increases at large y^* (the magnitude of ω_z increases) tends to support the existence (in some cases) of hairpin vortices, their legs being connected at their top ends at large y^*.

7.2. *Conditioning related to the large-scale organized motion*

The properties of the organized motion of the far wake in the (x, y)-plane have been reported extensively (e.g. Townsend 1979; Mumford 1983; Browne *et al.* 1986; Antonia *et al.* 1987*a*; Bisset *et al.* 1990; Ferré & Giralt 1989*a*), but the complete vorticity vector was not available previously. In this section we examine the most probable (i.e. most commonly occurring) distribution of vorticity in relation to the large-scale organized motion, i.e. spanwise rotating structures that generally occupy most of one side of the wake.

After it was confirmed that WAG detections in the v_0 signal were similar to those obtained previously in v-signals (e.g. Bisset *et al.* 1990), subsets of negative-slope v_0 WAG detections, separated from other detections by the most probable time interval $\Delta t U_1/L = 3.2 \pm 10\%$, were selected (step 1). In sectional streamline patterns these detections correspond to saddle points between adjacent structures, and therefore two successive detections delineate (in x) the region occupied by a spanwise structure. Detections in v-signals from two ×-probes separated in the y-direction generally occur at about the same time (Bisset *et al.* 1990), which allows the present results at different y^* to be aligned with each other. Histograms of time intervals between vorticity detections and v_0-detections were examined to see whether vorticity detections tend to occur within any particular part of the spanwise structure. The time interval histograms for detections of negative peaks in ω_z showed distinct tendencies at all values of y^*, whereas the histograms for ω_x and ω_y showed

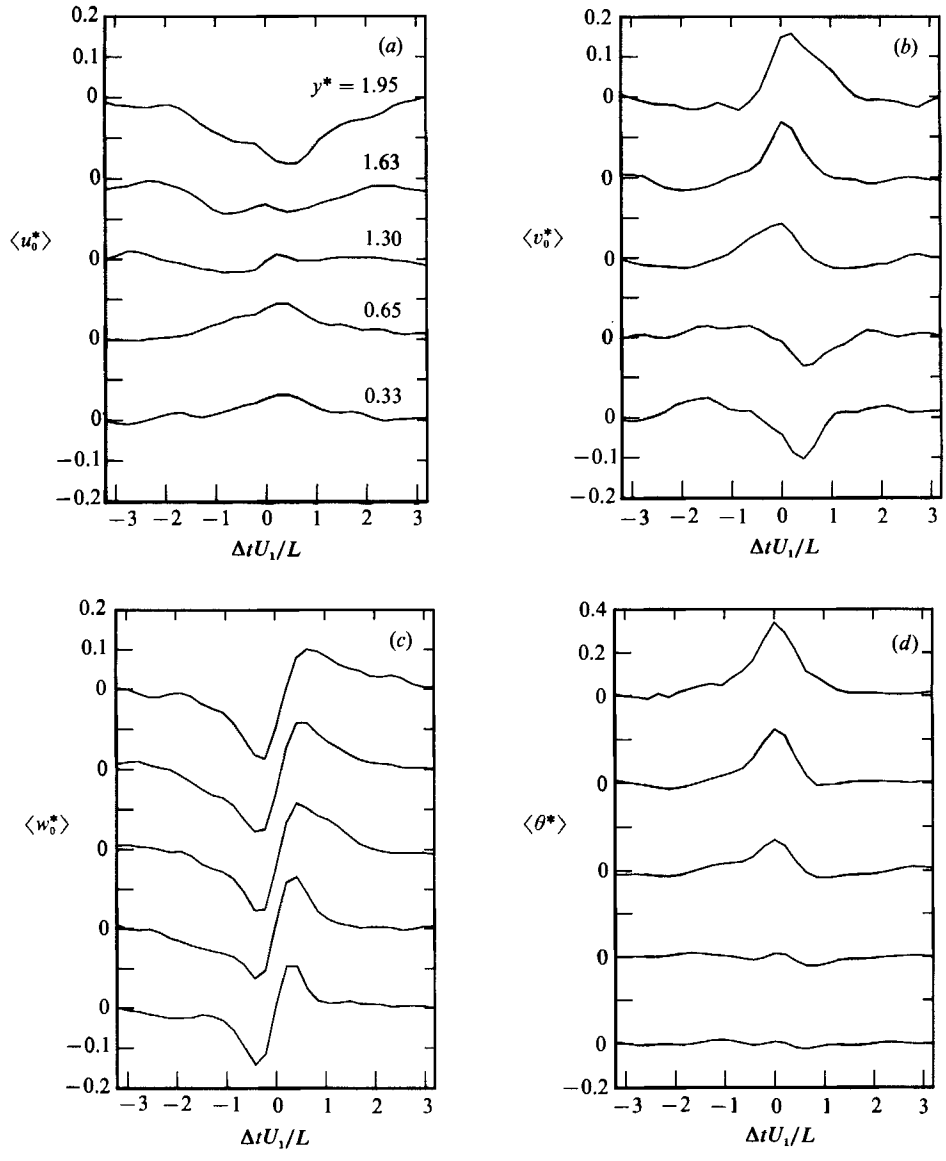

FIGURE 8(*a–d*). For caption see facing page.

distinct tendencies only at large y^*. Two of the histograms for negative ω_z peaks are shown in figure 10. The ω_z detections rarely occur at the same time as WAG detections. At $y^* = 0.33$ (not shown) and 0.65 there is a tendency for detections to occur at $\Delta t U_1/L \approx 1$, while at $y^* = 1.30$ and above they occur much more often at $\Delta t U_1/L \approx 2$. Further selection from the step 1 detection subsets was made using the criterion that ω_z detections should fall within the above-mentioned histogram peaks. The sizes of the initial sets of WAG detections were reduced to about 35% by the criterion of most probable separation between successive WAG detections (step 1), and further reduced to 10%–15% by the criterion of ω_z detections at the most probable relative times (step 2). A considerably larger proportion of the original detections would satisfy criteria only slightly different from those used for the

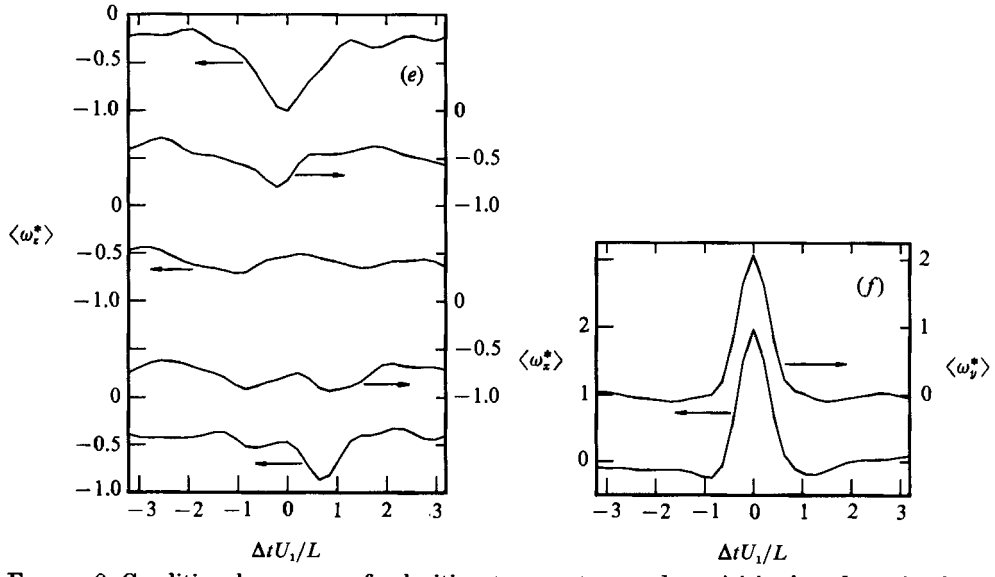

FIGURE 8. Conditional averages of velocities, temperature and vorticities based on simultaneous detections of positive ω_x and ω_y. (*a*) $\langle u_0^* \rangle$; (*b*) $\langle v_0^* \rangle$; (*c*) $\langle w_0^* \rangle$; (*d*) $\langle \theta^* \rangle$; (*e*) $\langle \omega_z^* \rangle$; (*f*) $\langle \omega_x^* \rangle$ and $\langle \omega_y^* \rangle$ at $y^* = 1.30$.

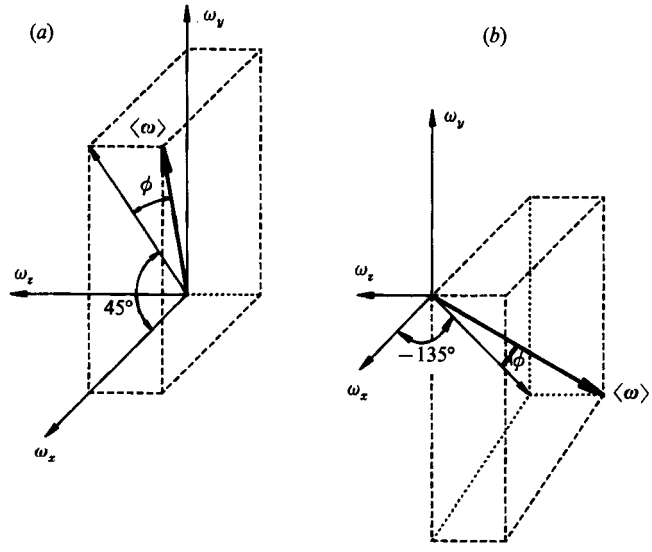

FIGURE 9. Conditional vorticity vector based on simultaneous detections of ω_x and ω_y: (*a*) positive ω_x and ω_y; (*b*) negative ω_x and ω_y.

selected subsets, however, so the results are representative of a significant part of the flow.

Conditional averages of ω_x, ω_y and w_0 based on these detection subsets are essentially zero owing to symmetry, but these are the most interesting quantities in the present context. A rational basis on which to split the data into its two 'symmetrical' halves was sought. The sign of ω_x, ω_y or w_0 at some particular time relative to the detection is a simple criterion, but it will be meaningful only if the quantity tends to be either strongly positive or strongly negative at that time. In order to determine the times at which absolute values of ω_x and ω_y are large,

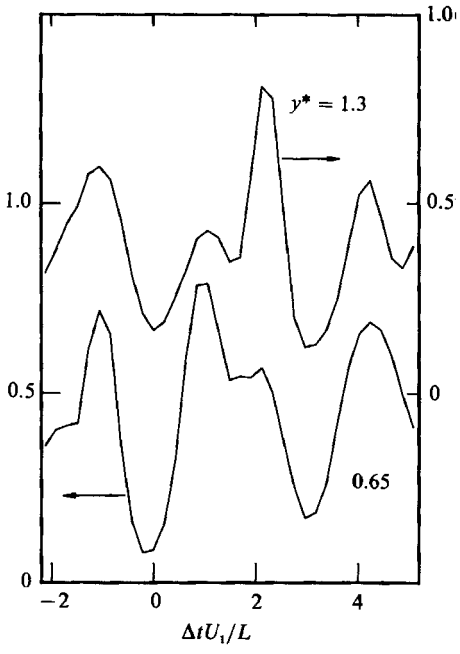

FIGURE 10. Histograms of time delays between detections of negative peaks of ω_z and WAG detections in v_0 at $\Delta t = 0$, when WAG detections also occur at $\Delta tU_1/L = 3.2$.

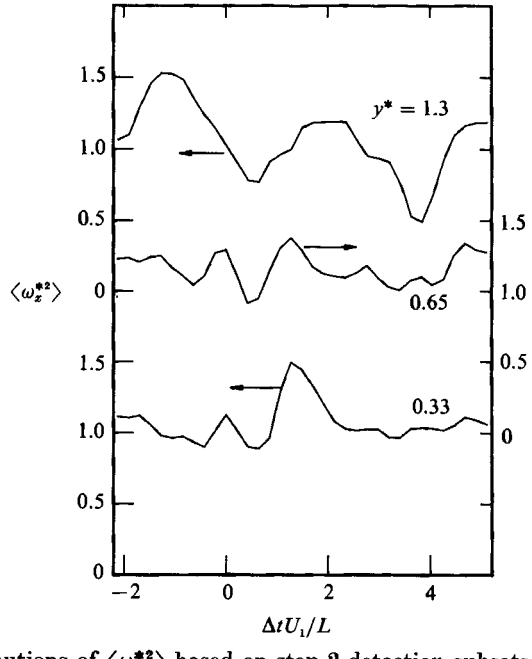

FIGURE 11. Distributions of $\langle \omega_z^{*2} \rangle$ based on step 2 detection subsets, i.e. WAG detections in v_0 at $\Delta tU_1/L = 0$ and 3.2 with $-\omega_z$ detections at their most probable locations (cf. figure 10).

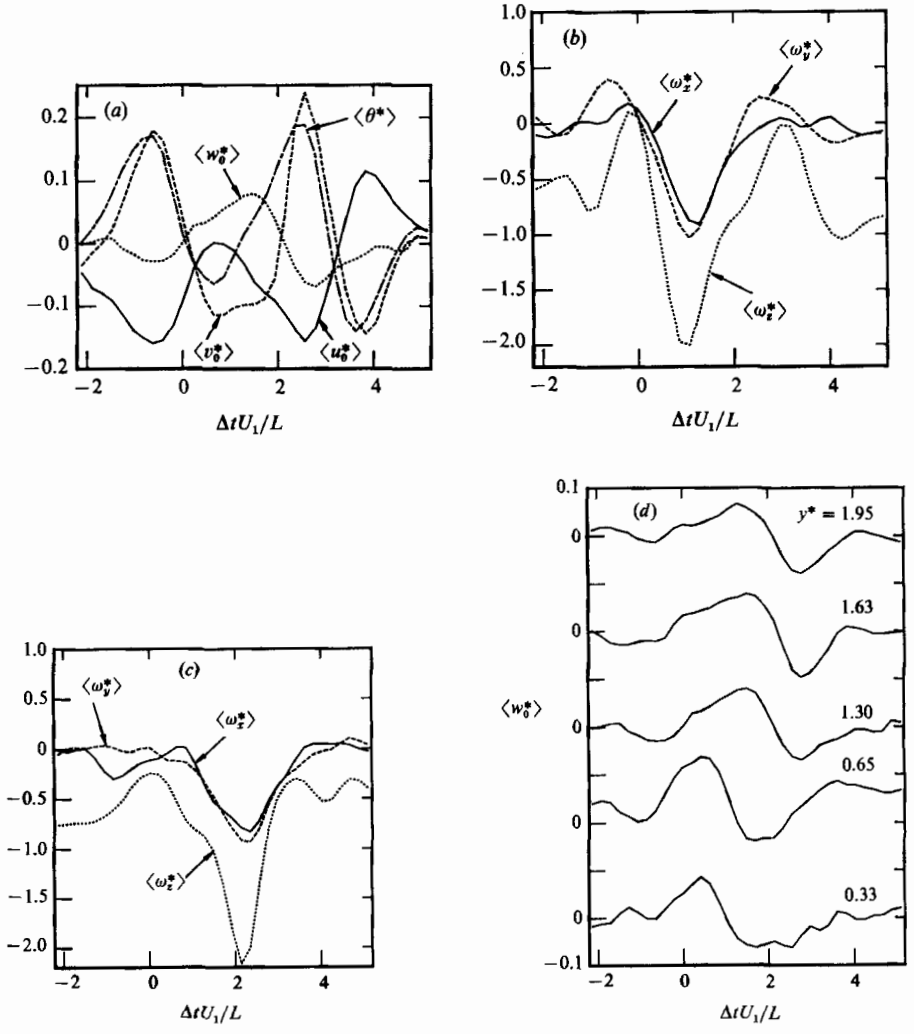

FIGURE 12. Conditional averages of velocities, temperature and vorticities based on step 2 detection subsets (see text) with ω_x and ω_y both negative: (*a*) $\langle u_0^* \rangle$, $\langle v_0^* \rangle$, $\langle w_0^* \rangle$ and $\langle \theta^* \rangle$ at $y^* = 1.3$; (*b*) $\langle \omega_x^* \rangle$, $\langle \omega_y^* \rangle$, $\langle \omega_z^* \rangle$ at $y^* = 0.65$; (*c*) $\langle \omega_x^* \rangle$, $\langle \omega_y^* \rangle$, $\langle \omega_z^* \rangle$ at $y^* = 1.3$; (*d*) $\langle w_0^* \rangle$ for several values of y^*.

conditional averages of ω_x^2 and ω_y^2 were calculated using the step 2 detections. Reasonably distinct peaks were found for all y-values (except perhaps $y^* = 0.65$), as shown for $\langle \omega_x^2 \rangle$ in figure 11 ($\langle \omega_y^2 \rangle$ is similar). The peaks are close to (but not coincident with) the peaks in the ω_z detection histograms (figure 10). Figure 11 also indicates that significant values of ω_x and ω_y can occur anywhere relative to the step 2 detections for the lower values of y^*. The sign of the short-time average value of ω_x for a duration corresponding to the peak in $\langle \omega_x^2 \rangle$ was used as the criterion for splitting the step 2 detections into two symmetrical subsets, and those subsets were further split according to the sign of ω_y in the region of maximum $\langle \omega_y^2 \rangle$. As could be expected from the correlation coefficient $\rho_{\omega_x \omega_y}$ (figure 3), the subsets of detections where ω_x and ω_y have opposite signs are generally smaller than those where they have the same sign, especially at large y^*, and results for only the subsets of same sign are presented here.

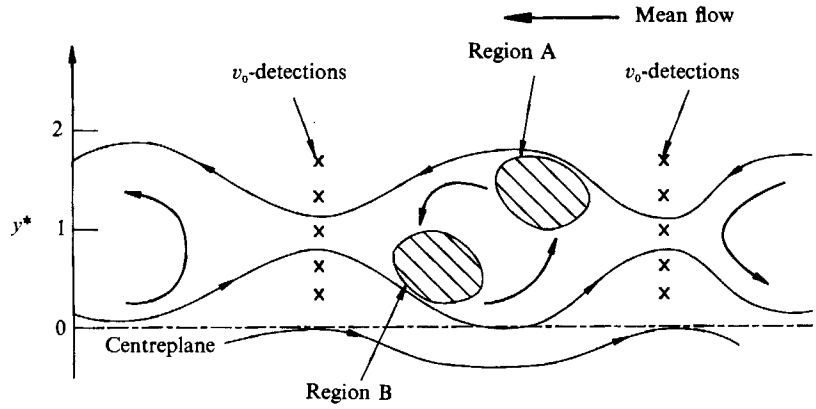

FIGURE 13. Schematic summary of conditional averages. Region A contains relatively warm, low-momentum fluid moving rapidly upwards, with large $-\omega_z$, and moderate levels of ω_x and ω_y which usually have the same sign. Region B contains relatively cold, high-momentum fluid moving downwards, with large $-\omega_z$, and moderate levels of ω_x and ω_y which can have the same or opposite sign. The temperature levels in Regions A and B are quite similar, likewise the streamwise momentum levels, although they are both different from the immediate surroundings.

Results for $\langle u_0 \rangle$, $\langle v_0 \rangle$ and $\langle \theta \rangle$ are shown in detail for $y^* = 1.30$ in figure 12(*a*), and results at all y^*-values are summarized in the sketch in figure 13. Conditional averages of the vorticity components for the cases where ω_x and ω_y are both negative are shown in figure 12(*b*) for $y^* = 0.65$ ($y^* = 0.33$ is similar) and figure 12(*c*) for $y^* = 1.30$ ($y^* = 1.63$ and 1.95 are similar). Figure 12(*d*) shows $\langle w_0 \rangle$ at all y^*-values. The vorticity vectors $\langle \boldsymbol{\omega} \rangle$ at the point of maximum $\langle \omega_z \rangle$ are similar to those shown in figure 9, except that the angle ϕ is approximately 60°, much larger than the values obtained using ω_x and ω_y detection. As for the previous results, conditionally averaged velocity signals from the individual ×-probes are consistent with the presence of a vortex rather than a local shear layer.

8. Discussion

It is well established from both flow visualizations (e.g. Cimbala, Nagib & Roshko 1988) and spectra of velocity fluctuations that the frequency of vortical structures decreases and their mean size increases with downstream development of the wake. Antonia, Browne & Fulachier (1987*b*) found that in the far wake the mean wavelength of dominant structures satisfies self-preservation, i.e. it increases as $x^{\frac{1}{2}}$. Spectra of fluctuations also show that different frequencies and scales coexist while larger scales gradually grow in importance relative to smaller scales. Because the large-scale structures are essentially space filling, the remnants of smaller-scale structures must be incorporated into the largest ones in some sense, although not necessarily in a highly deterministic vortex pairing process. The results from the previous section can be explained in terms of downstream development of the wake. No assumption of any particular mechanism (e.g. hydrodynamic instability of the mean velocity profile) for the generation of new structures is necessary.

The WAG detections in v-signals arise from the large, energetic structures occupying one side of the wake, non-uniform (perhaps quite short) in the spanwise (z) direction. Parts of smaller-scale structures near the upstream boundaries of the large ones are lifted up and stretched downstream, as indicated in figure 14(*a*), which

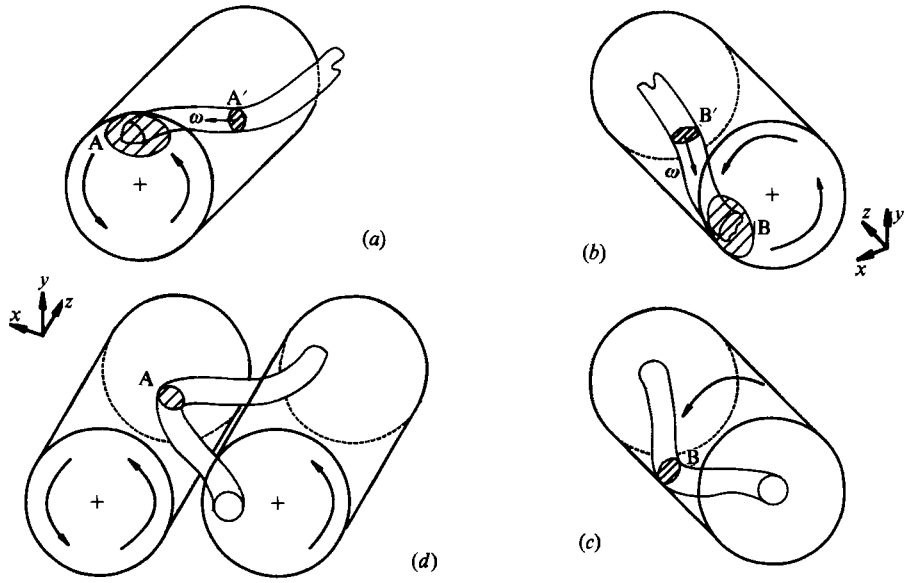

FIGURE 14. Possible configurations of large-scale spanwise vortices and smaller vortices. (*a*) Part of a smaller structure lifted and stretched at the upstream end of a large structure (Region A); ω_x and ω_y are strongest in Region A′. (*b*) Part of a smaller structure lowered and stretched at the downstream end of a large structure (Region B); ω_x and ω_y are strongest in Region B′. (*c*) The structures in (*b*) and their mirror image joined to form a lowered vortex loop. (*d*) The structures in (*a*) and their mirror image joined to form a raised vortex loop, with its legs attached to an upstream large structure.

makes ω_x and ω_y large and of the same sign. Here the small structures are mainly surrounded by ambient-temperature free-stream fluid which has small ω_x and ω_y, and therefore the observed ω_x and ω_y in region A are highly correlated with the presence of the large structures. When detection is based on ω_x and ω_y, as in §7.1, the region A′ (figure 14*a*) with the largest magnitudes of $\langle\omega_x\rangle$ and $\langle\omega_y\rangle$ is detected. The sketches in figure 14 are not meant to imply that structures have precisely defined boundaries, nor that they are exactly the shapes shown, but are only an attempt to show the general relationship between structures of different sizes. Near the downstream boundaries of large structures, parts of small structures are pushed downwards towards the centreline of the wake (figure 14*b*). Here in region B (figures 13 and 14*b*) they are surrounded by warm fluid already containing structures of all sizes, and they may be influenced by large structures from the other side of the wake as well, so the measured ω_x and ω_y are not strongly correlated with each other or with other quantities including scalar fluctuations such as temperature. Large values of ω_x and ω_y can still be detected, however, which would correspond to region B′ in figure 14(*b*). Although region B contains the locally strongest ω_z values, ω_x and ω_y are uncorrelated with the large spanwise structures at small y, and are probably associated mainly with smaller (and mostly older) structures undergoing distortion. The curves for $\langle w_0\rangle$ based on the two detection methods, figures 8(*c*) and 12(*d*), show considerable similarity after allowing for the opposite signs of $\langle\omega_y\rangle$ in the two cases. The curves in figure 8(*c*), ω_x and ω_y detection, are larger and sharper, but in figure 12(*d*) there is additional information about the alignment of $\langle w_0\rangle$ relative to the large structures.

Since the structures in figure 14(*b*) and their mirror image occur equally often, it

is quite likely that they sometimes occur side by side, thus forming the lowered vortex loop shown in figure 14(*c*). Similarly, the structures in figure 14(*a*) and their mirror image may form the raised vortex loop shown in figure 14(*d*). In this case either or both of the legs of the loop may join onto an upstream large structure as sketched, a braid-like arrangement of shear-aligned ω_x, ω_y vortices connecting relatively larger spanwise vortices, similar to the mixing-layer braid discussed by Corcos & Lin (1984). In general, individual realizations of the suggested structures would be distorted or incomplete, and also their planes of symmetry, where present, would not coincide with the measurement probe. Hayakawa & Hussain (1989) measured ω_y and ω_z (separately) using rakes of $\times$-wires in a cylinder wake at $x = 20d$ and $40d$. They suggested that their observations could be explained by distortion of the main spanwise structures, distorted horseshoe-like structures, and/or longitudinal ribs (their figures 13, 14 and 20 respectively), and indicate that the three cases are not entirely different.

By examining instantaneous and conditionally averaged vortex lines in numeral simulations of channel flow, Kim & Moin (1986) identified two distinct horseshoe-shaped structures, one with a raised tip surrounded by rising low-momentum fluid, the other with a lowered tip surrounded by descending high-momentum fluid. They conjectured that these structures also exist in free-shear flows. The present results support the existence of similar structures in the far wake. At large y, where turbulence is intermittent, the raised vortex loops are most common, but at small y, where the flow is fully turbulent, there is a mixture of lowered loops, the legs of raised loops, and the remnants of other small-scale structures. Further downstream in the wake, even larger structures begin to form, which in their turn distort, stretch, and eventually destroy the identity of the structures that are currently largest. It is important to note that this picture does not contradict the idea that there can be, instantaneously, a cascade of energy from larger vortical structures to smaller ones; in fact, it shows one way in which the mechanisms of vortex stretching (and hence the dissipation of energy at small scales) could operate, consistent with the observed increase in scale with downstream distance in the self-preserving far wake. Further testing of these hypotheses ideally requires the simultaneous measurement, with probes that have good spatial resolution, of all components of vorticity at several points in space.

Recently, Bisset *et al.* (1990) constructed a kinematic model of the far wake in the (x, y)-plane based on modified Rankine vortices. After assuming a certain arrangement of these spanwise vortices in the z-direction, distributions of u and w were obtained in (x, z)-planes by means of the continuity equation. The result was a distinct pattern of vortices with circulation in (x, z)-planes and a scale one half that of the basic spanwise vortices. Bisset & Antonia (1989) applied the WAG algorithm to detect increases in u-signals at the same y^* value ($y^* \approx 1$) in two experiments with a rake of eight $\times$-probes, one in the (x, y)-plane and the other in the (x, z)-plane. As could be expected from the shape of the $\langle u_0 \rangle$ curve in figure 12(*a*), large spanwise vortices were detected in the (x, y)-plane, but the conditional average result in the (x, z)-plane was a pattern of $\langle \omega_y \rangle$ vortices very similar to the result from the kinematic model. The directions of circulation near the upstream and downstream edges of the spanwise structures correspond to the directions for raised and lowered vortex loops respectively. The pattern in (x, z)-planes also looks like a cut through double-roller structures, which is a strong indication that large spanwise vortices and double rollers are in fact two views of the same highly three-dimensional structure. Nevertheless, instantaneous distributions of ω_y in (x, z)-planes (Bisset & Antonia

1989) tend to support the continuing existence of slightly smaller, more intense vortices whose locations are only partly determined by the presence of three-dimensional large structures, and which correspond to the smaller, older structures discussed in this paper and depicted in figure 14.

9. Conclusions

Simultaneous measurements of all three components of large-scale vorticity, along with temperature fluctuations, have been made in the self-preserving far wake of a slightly heated cylinder. Correlation coefficients, r.m.s. values, and p.d.f.s. of vector angles all indicate that the behaviour of ω_x is quite similar to that of ω_y, although ω_x is a little stronger in the outer wake. The projection of vorticity in the (x, y)-plane is predominantly at 45° or −135° to the x-axis. The r.m.s. values of ω_z fluctuations are larger than those of ω_x and ω_y, however. Distributions of r.m.s. values of θ and the vorticity magnitude ω have very similar shapes, and $\rho_{\omega\theta}$ is large except near the centreplane. Spanwise vorticity is associated with warm fluid in the outer part of the wake, and with cold fluid towards the centreplane.

Two detection techniques were applied. The first focuses on simultaneous peaks in ω_x and ω_y, and the resulting conditional averages show that the vorticity vector often makes only a small angle (of order 10°) to the (x, y)-plane, except at large y. The second technique detects large-scale spanwise structures and separates them into symmetrical subsets with either positive or negative ω_x or ω_y. At small y, ω_x and ω_y are not especially correlated with the large structures or with ω_z or θ, while at large y there is a close relationship between these quantities. Spanwise vorticity is always correlated with large spanwise structures. The conditional vorticity vector associated with large structures makes an angle to the (x, y)-plane of order 60° at the positions where all three conditional vorticity components are well defined. Results for the spanwise velocity $\langle w_0 \rangle$ are fairly similar for the two methods. The magnitudes of $\langle w_0 \rangle$ and $\langle v_0 \rangle$ are of the same order, implying that the observed structures are a very significant source of spanwise velocity fluctuations.

The results from detection and conditional averaging can be explained in terms of the downstream development of successively larger scales in the self-preserving far wake, an explanation that links the concepts of double-roller and spanwise entrainment structures. The larger, initially spanwise structures distort and stretch the smaller, older structures, causing the appearance of raised vortex loops at large y, their legs being nearly parallel to the (x, y)-plane. Cuts through these look like cuts through double rollers, although it is shown elsewhere that large three-dimensional spanwise structures may induce some of the double-roller-type circulation directly (Bisset & Antonia 1989; Bisset *et al.* 1990). At small y, there is a mixture of lowered vortex loops, the legs of raised loops and other parts of smaller structures, not correlated with temperature fluctuations. Since ω_z is mainly associated with large structures, it is ω_x and ω_y that are intensified by the stretching of smaller vortical structures.

The contribution of Dr L. W. B. Browne to the experiment is much appreciated. The financial support of the Australian Research Council is gratefully acknowledged. D. Britz also wishes to acknowledge support from the Danish Technical-Scientific Research Council journal number 16-4554M. We are grateful to R. Beach of the SLAC for providing the software package UGSYS.

REFERENCES

ANTONIA, R. A., BROWNE, L. W. B., BISSET, D. K. & FULACHIER, L. 1987*a* A description of the organized motion in the turbulent far-wake of a cylinder at low Reynolds number. *J. Fluid Mech.* **184**, 423–444.

ANTONIA, R. A., BROWNE, L. W. B. & FULACHIER, L. 1987*b* Average wavelength of organised structures in the turbulent far wake of a cylinder. *Expts. Fluids* **5**, 298–304.

ANTONIA, R. A., BROWNE, L. W. B. & SHAH, D. A. 1988 Characteristics of vorticity fluctuations in a turbulent wake. *J. Fluid Mech.* **189**, 349–365.

ANTONIA, R. A. & FULACHIER, L. 1989 Topology of a turbulent boundary layer with and without wall suction. *J. Fluid Mech.* **198**, 429–451.

BISSET, D. K. & ANTONIA, R. A. 1989 Experimental study of three-dimensional aspects of organised motion in turbulent flows. *Proc. Tenth Australasian Fluid Mechanics Conference, Melbourne.*

BISSET, D. K., ANTONIA, R. A. & BROWNE, L. W. B. 1990 Spatial organization of large structures in the turbulent far wake of a cylinder. *J. Fluid Mech.* [to appear].

BROWNE, L. W. B., ANTONIA, R. A. & BISSET, D. K. 1986 Coherent structures in the far-field of a turbulent wake. *Phys. Fluids* **29**, 3612–3617.

CIMBALA, J. M., NAGIB, H. M. & ROSHKO, A. 1988 Large structure in the far wakes of two-dimensional bluff bodies. *J. Fluid Mech.* **190**, 265–298.

CORCOS, G. M. & LIN, S. J. 1984 The mixing layer: deterministic models of a turbulent flow. Part 2. The origin of the three-dimensional motion. *J. Fluid Mech.* **139**, 67–95.

DEISSLER, R. G. 1969 Direction of maximum turbulent vorticity in a shear flow. *Phys. Fluids* **12**, 426–427.

FERRÉ, J. A. & GIRALT, F. 1989*a* Pattern-recognition analysis of the velocity field in plane turbulent wakes. *J. Fluid Mech.* **198**, 27–64.

FERRÉ, J. A. & GIRALT, F. 1989*b* Some topological features of the entrainment process in a heated turbulent wake. *J. Fluid Mech.* **198**, 65–78.

FERRÉ, J. A., GIRALT, F. & ANTONIA, R. A. 1989 Evidence for double-roller eddies in a turbulent wake from two-component velocity measurements. *Proc. Seventh Symposium on Turbulent Shear Flows, Stanford.*

GRANT, H. T. 1958 Large eddies of turbulent motion. *J. Fluid Mech.* **4**, 149–190.

HAYAKAWA, M. & HUSSAIN, A. K. M. F. 1989 Three-dimensionality of organized structures in a plane turbulent wake. *J. Fluid Mech.* **206**, 375–404.

KEFFER, J. F. 1965 The uniform distortion of a turbulent wake. *J. Fluid Mech.* **22**, 135–159.

KIM, J. & MOIN, P. 1986 The structure of the vorticity field in turbulent channel flow. Part 2. Study of ensemble-averaged fields. *J. Fluid Mech.* **162**, 339–363.

MOIN, P. & KIM, J. 1985 The structure of the vorticity field in turbulent channel flow. Part 1. Analysis of instantaneous fields and statistical correlations. *J. Fluid Mech.* **155**, 441–464.

MUMFORD, J. C. 1983 The structure of the large eddies in fully developed turbulent shear flows. Part 2. The plane wake. *J. Fluid Mech.* **137**, 447–456.

PAYNE, F. R. & LUMLEY, J. L. 1967 Large eddy structure of the turbulent wake behind a circular cylinder. *Phys. Fluids Suppl.* S194–S196.

ROSHKO, A. 1976 Structure of turbulent shear flows: a new look. *AIAA Paper* 76–78, presented at *AIAA 14th Aerospace Sciences Meeting, Washington.*

SAVILL, A. M. 1979 Effects on turbulence of curved or distorting mean flow, Ph.D. thesis, University of Cambridge.

TOWNSEND, A. A. 1979 Flow patterns of large eddies in a wake and in a boundary layer. *J. Fluid Mech.* **95**, 515–537.